JOURNAL OF SOLID STATE CHEMISTRY 114, 211–218 (1995)

Imaging of La/Sr Vacancy Defects in $La_{0.8}Sr_{0.2}MnO_3$ by High-Resolution Transmission Electron Microscopy

H. Cerva

Siemens AG, Research Laboratories, Otto Hahn Ring 6, D-81730 München, Germany

Received December 27, 1993; in revised form May 12, 1994; accepted May 16, 1994

Defects on (100) planes of $La_{0.8}Sr_{0.2}MnO_3$, approximately 25 nm in size, were investigated by high-resolution transmission electron microscopy (HREM). A systematic comparison of experimental ⟨100⟩ and ⟨110⟩ HREM images of the defects with calculated images for defect models with vacant La/Sr or Mn atom columns was carried out. It turned out that the defects consist of pure La/Sr vacancy defects, one atomic layer thick, with zero cation occupancy. Due to the high density of defects the concentration of La/Sr vacancies corresponds to approximately 1 at% La/Sr. Under the chosen imaging conditions ⟨110⟩ HREM images are sensitive to defects with 75% La/Sr occupancy.

1. INTRODUCTION

Sr-doped lanthanum manganites $La_{1-x}Sr_xMnO_3$ ($0.1 \leq x \leq 0.4$) have a pseudocubic perovskite structure and show several interesting physical properties. The partial substitution of La^{3+} by divalent Sr^{2+} leads to the presence of 3- and 4-valent Mn ions due to charge compensation. Neighboring Mn^{3+} and Mn^{4+} ions cause charge-transport and spontaneous magnetization via a double-exchange mechanism (1). This causes a magnetoresistance effect over the temperature range where ferromagnetism occurs (Curie temperature ≈60°C). $La_{0.8}Sr_{0.2}MnO_3$ reveals also electronic semiconducting properties which makes it a good candidate as an air electrode for high-temperature oxide fuel cells (2–4). Oxidative nonstoichiometry is particularly well known in orthorhombic perovskite-related $LaMnO_{3+\delta}$ which leads to interstitial oxygen (5). Charge compensation is obtained via oxidation of the Mn ions. A stoichiometric Mn cation and O anion sublattice is obtained in this material by the formation of a second phase, i.e., La_2O_3, and the formation of La vacancies to yield $La_{1-x}MnO_3$ (5).

The objective of this paper is to study the image contrast of planar nanometer-size vacancy defects in $La_{0.8}Sr_{0.2}MnO_3$ grains by high-resolution transmission electron microscopy (HREM). Since the physical properties in perovskite and perovskite-related materials are strongly influenced by cation and anion vacancies the microstructural characterization of vacancy defects is important for material technology development (6). A systematic comparison of experimental and calculated HREM images is described and specific HREM imaging conditions are given which can be used for La/Sr vacancy defect analysis in $La_{0.8}Sr_{0.2}MnO_3$ in the future.

2. EXPERIMENTAL

A sample of $La_{0.8}Sr_{0.2}MnO_3$ was synthesized by mixing La_2O_3, $SrCO_3$, and MnO_2 powders and a first solid-state reaction step at 1200°C. The pressed powders were sintered in air to dense pellets at 1300°C (7).

The crystal structure of $La_{0.8}Sr_{0.2}MnO_3$ at room temperature is trigonal (R-3c, space group 167) and may be described at room temperature with a pseudocubic cell $a = 0.387$ nm, $\alpha \approx 89.55°$ as determined with a high-temperature powder diffractometer (8, 9). In this work it is described by a cubic unit cell with $a = 0.386$ nm (perovskite space group 221). All indices in this work correspond to the cubic cell.

A JEOL 200CX transmission electron microscope (TEM) was used for conventional bright-field imaging whereas HREM images were recorded in a JEOL 4000EX microscope at 400 kV (having a spherical aberration constant $C_S = 1$ mm yielding a point-to-point resolution of 0.175 nm). High-resolution multislice simulations were carried out with the EMS programs of Stadelmann (10) using the following microscope parameters: acceleration voltage 400 kV, spherical aberration constant $C_S = 1$ mm, defocus spread $\Delta = 13$ nm, and semiconvergence angle $\alpha = 0.9$ mrad, objective lens aperture diameter 20 nm^{-1}. Optical diffractograms were recorded from the negatives of the amorphous rim of the TEM specimen. The objective lens defocus of the experimental images was then determined from the optical diffractograms by using the method described by Thon (11). TEM specimen preparation was carried out by mechanical grinding and conventional Ar ion beam thinning. Ion beam thinning was carried out

0022-4596/95 $6.00

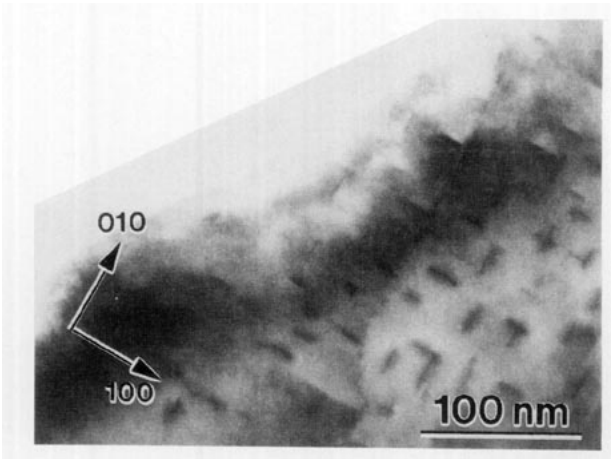

FIG. 1. ⟨100⟩ aligned bright-field image of a $La_{0.8}Sr_{0.2}MnO_3$ grain with planar defects on {100} planes.

with a shallow incidence angle (10°), low voltage (3 kV), and at liquid nitrogen temperature. No ion-beam-induced damage was observed. $La_{0.8}Sr_{0.2}MnO_3$ grains which were produced differently than mentioned above did not reveal the defects described above. Hence, the observed La/Sr defects were found to be inherent in the investigated $La_{0.8}Sr_{0.2}MnO_3$ material and not a preparation artifact.

3. RESULTS

3.1. *Conventional TEM Imaging*

Bright-field images of $La_{0.8}Sr_{0.2}MnO_3$ (LSM) grains, which were sintered as described above, reveal fine dark lines when the electron beam is oriented parallel to a ⟨100⟩ axis. These lines are approximately 25 nm long, running in perpendicular ⟨100⟩ directions (Fig. 1). Such a contrast is typical for a planar defect with its habit plane oriented parallel to the electron beam. When the grains are tilted off the ⟨100⟩ zone axis so that the habit planes of the defects lie oblique to the electron beam no fringe contrast is observed. Fringe contrast would be typical for, e.g., a stacking fault, or stem from Moiré fringes due to the overlapping different lattices of a platelike precipitate and the matrix. Since the LSM grains in the ceramic body have no preferred orientation and several grains were studied, it is concluded that the observed defects lie on all three equivalent {100} planes. The ⟨100⟩-oriented bright-field images in Figs. 2a and 2b show the same defect recorded with the objective lens over- and underfocused, respectively. The defect appears with bright and dark Fresnel fringes which reverse contrast when changing from over- to underfocus. This behavior makes it possible to study the mean atomic potential of the interior of the defect. As can be derived from the bright/dark/bright fringes in the overfocused image (Fig. 2a) and the dark/bright/dark fringes in the underfocused image (Fig. 2b), the defect must have a lower density and/or a lower atomic number than the surrounding LSM matrix. In order to study the nature of the defects more closely they were imaged under high resolution.

3.2. *⟨100⟩ HREM Imaging*

In the ⟨100⟩ zone axis the metal atoms are viewed as separate columns of *A* cations (La/Sr) and *B* cations (Mn). Two-thirds of the oxygen atoms form two pure oxygen columns lying in-between the *A* cation columns while the other third lies within the *B* cation column alternating with the Mn atoms. A–A cation distances correspond to {100} lattice plane spacings of 0.386 nm while *A–B* cation distances correspond to {110} lattice plane spacings of 0.2729 nm. The thinnest specimen regions, i.e., at the edge of a TEM sample, were chosen to image the defects since there the HREM contrast arising at Scherzer focus ($\Delta f = -49$ nm) can be interpreted directly with help of the projected potential, i.e., cation columns appear as dark dots and tunnels in the crystal structure are imaged as bright dots. The oxygen atoms are usually neglected as weak scatterers, but their influence on the HREM contrast depends strongly on specimen thickness, i.e., on dynamical effects. Figure 3 displays simulated images calculated by the multislice method (slice thickness 0.0965 nm, sampling 128 × 128) for the thickness range $1.2 \leq t \leq 5.8$ nm, and the defocus range $-50 \leq \Delta f \leq -15$ nm. In the right part of Fig. 3 the ⟨100⟩ projected crystal structure

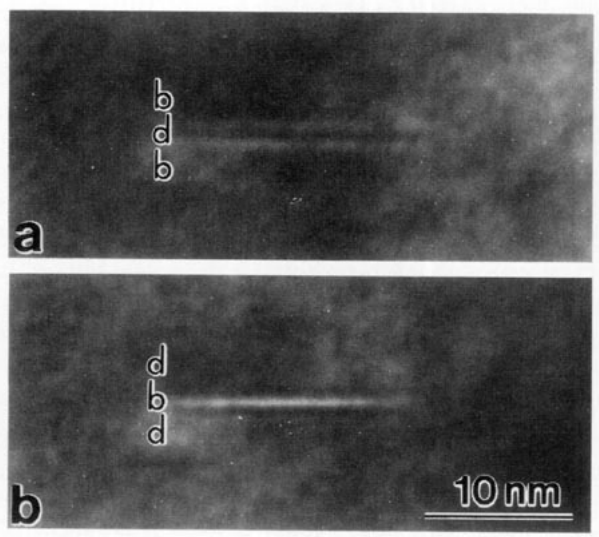

FIG. 2. ⟨100⟩ aligned bright-field images of the same defect on a {100} plane (a) giving rise to *b*right/*d*ark/*b*right Fresnel fringes at overfocus, and (b) to *d*ark/*b*right/*d*ark fringes at underfocus.

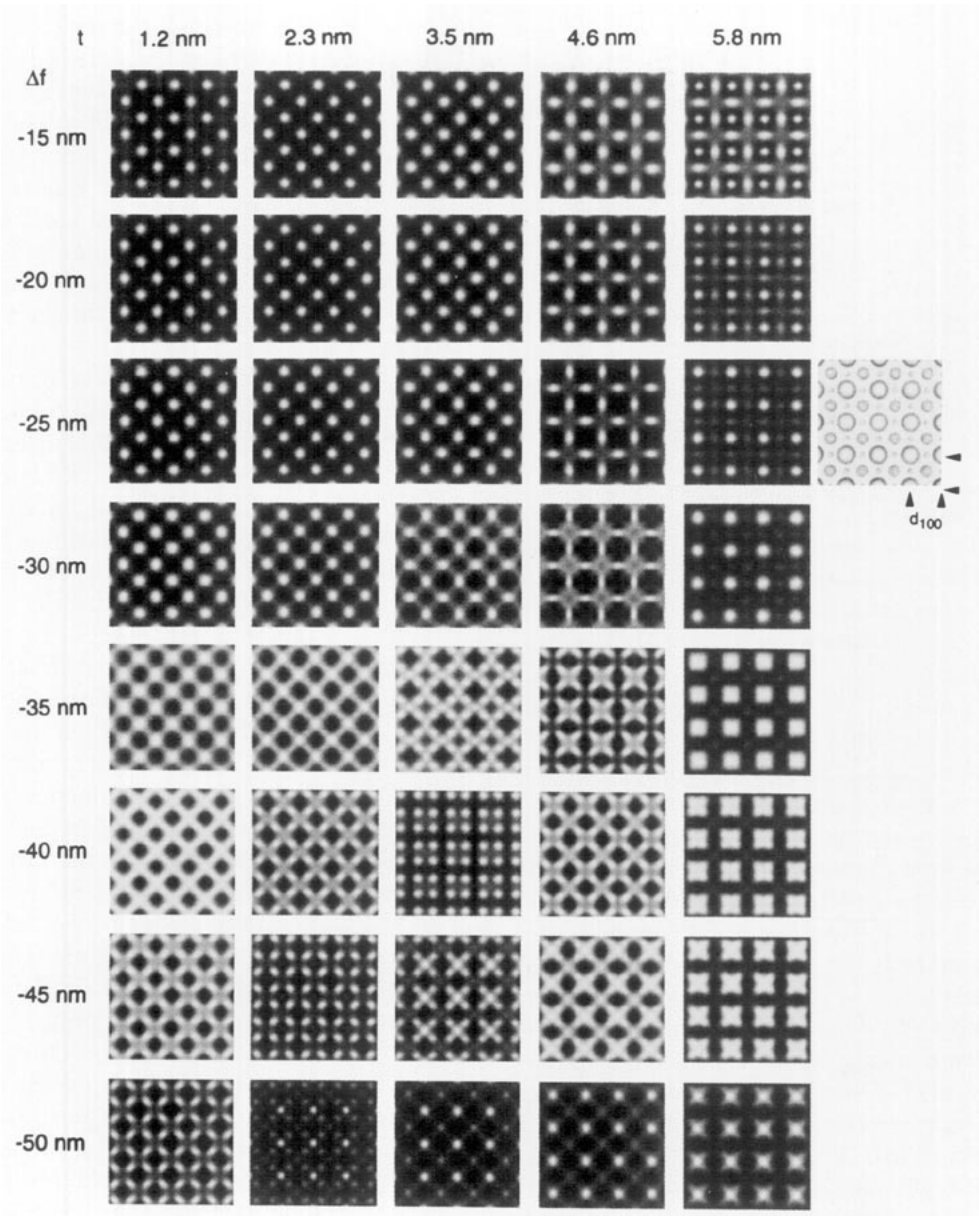

FIG. 3. Calculated ⟨100⟩ HREM images of the perfect crystal for various defoci Δf and specimen thicknesses t. The unit cell of the ⟨100⟩ projected $La_{0.8}Sr_{0.2}MnO_3$ structure can be seen to the right of the simulated images. Large atoms, La and Sr; medium atoms, Mn; and small atoms, O.

is shown with the positions of the atomic columns corresponding to those used in the simulations. Close at Scherzer focus ($\Delta f = -50$ nm) and for a thickness of $t = 1.2$ nm both cation columns are visible as black dots and tunnels as bright dots. However, the cation columns with the heavy La ($Z = 57$) and Sr ($Z = 38$) atoms do not appear as black dots larger than those of the cation columns with the light Mn ($Z = 25$) atoms. At thicknesses larger than $t = 1.2$ nm the images cannot be interpreted in terms of the projected potential at all. In the defocus range $-30 \leq \Delta f \leq -15$ nm the cation columns are also imaged dark and the tunnels bright but for a larger thickness range $1.2 \leq t \leq 3.5$ nm. In this defocus range, only at $t = 1.2$ nm does the La/Sr columns give rise to dark dots more pronounced than those of the Mn columns. At $t = 2.3$ nm the dark dots of both cation columns are indiscernible, whereas at $t = 3.5$ nm the dark dots of the Mn columns are clearly more pronounced.

The reason why images recorded at about $\Delta f = 20$ nm yield a contrast which agrees better with the projected

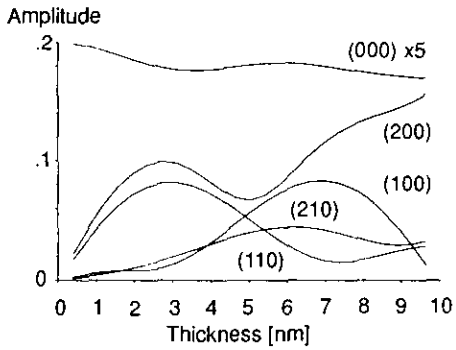

FIG. 4. Amplitudes of the main beams contributing to the ⟨100⟩ HREM image as a function of specimen thickness.

potential than that of images recorded at about $\Delta f = 45$ nm may be understood qualitatively as follows. The structure factor of the (100) reflection contains the difference of the atomic scattering amplitudes of the A and B cations in the perovskite structure, whereas the sum of both enters into the structure factor of the (110) reflection. Hence, a strong contribution of the ⟨100⟩ beams to the image will enhance differences between A and B columns. In Fig. 4 the amplitudes of the transmitted and the main diffracted beams are plotted versus thickness. For the specimen thicknesses under consideration, the amplitude of the (100) beam is 5–10 times smaller than the amplitude of the (110) or (200) beams. In Fig. 5 the contrast transfer functions are shown for $\Delta f = -20$ and -45 nm with the reciprocal spacings of the corresponding diffracted beams indicated. Contributions to the image contrast come from the (100), (110), and (200) beams. At a defocus of $\Delta f = -45$ nm the (110) beam mainly dominates since the amplitude of the (100) beam is so weak. This explains why the cation columns at $\Delta f = -45$ nm and $t = 1.2$ nm (Fig. 3) show the same contrast. At about $\Delta f = -20$ nm the contributions of the (110) and (200) beams are attenuated and the La/Sr columns show slightly more pronounced dark dots for $t = 1.2$ nm. For $t = 3.5$ nm the dark dots corresponding to the Mn columns appear more clearly.

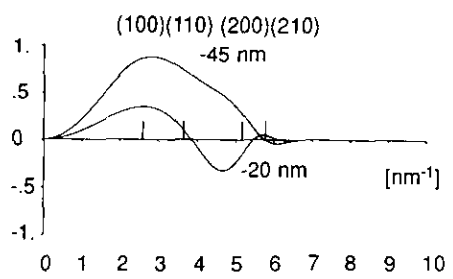

FIG. 5. Contrast transfer function for the defoci $\Delta f = -45$ and -20 nm. The reciprocal spacings corresponding to the main diffracted beams are indicated (400 kV, $C_S = 1$ mm, $\Delta = 13$ nm, $\alpha = 0.9$ mrad).

This is because the amplitudes of the (100) beams increase and those of the (110) beams decrease at this thickness.

Figure 6 shows a ⟨100⟩ HREM image of the thin edge of an LSM grain at low magnification. The inserted optical diffractogram obtained from the amorphous edge of the specimen reveals that the image was recorded at $\Delta f = -20 \pm 5$ nm. One defect denoted by A lies at the edge, whereas the other denoted by B lies in a slightly thicker specimen region. As the defects have a mean diameter of about 25 nm and the specimen thickness is ≤ 5 nm (as shown from image matching below) it is very probable that the defects extend completely throughout the thin TEM specimen. Both defects A and B may be recognized by a fine bright line running in a ⟨100⟩ direction. The bright line is more intense in case of defect B lying in the thicker specimen region. A higher magnification of defect B (Fig. 7a) shows that the cation columns cannot be distinguished by the dark dots. The contrast of the perfect crystal region corresponds perfectly to that in the simulations for $-25 \leq \Delta f \leq -15$ nm at a thickness of $t = 3.5$ nm in Fig. 3. In both images the fine bright line arises from a strongly increased intensity at the positions of one particular type of cation column. When interpreting the contrast on the basis of the projected potential the bright dots at the position of a cation column can be understood by a decreased concentration of cations in this particular atomic column. In the image of defect B (Fig. 7a) the Mn cation columns should be discernible from the La/Sr columns in the perfect crystal parts on both sides of the defect. This, however, is hardly possible in the higher magnified image (Fig. 7a). In the lower magnified image (at the arrow in Fig. 6) it becomes apparent from the contrast that the bright cation columns in the defect must correspond to La/Sr columns. Multislice simulations (slice thickness 0.386 nm, sampling 256 × 64) of supercells for a defect consisting of one complete atomic layer of La/Sr or Mn vacancies, respectively, were carried out. The best matched image for a La/Sr vacancy defect to the experimental image of defect B is given in Fig. 7b while the simulated image of a Mn vacancy defect is shown in Fig. 7c for comparison. From these results the observed defects on {100} planes must be envisaged as one-atomic-layer-thick precipitates of La/Sr vacancies. To corroborate the result the defects were also investigated in ⟨110⟩ projection.

3.3. ⟨110⟩ HREM Imaging

Also in ⟨110⟩ projection La/Sr and Mn cations occupy separate columns. Minimum distances of the same or different cation columns correspond to (110) and (200) lattice plane spacings, respectively. In the two-dimensional projection the (200) planes consist of alternating layers of La/Sr or Mn cations. This results in an *ABAB* stacking in the ⟨100⟩ direction with the cations on top of each other.

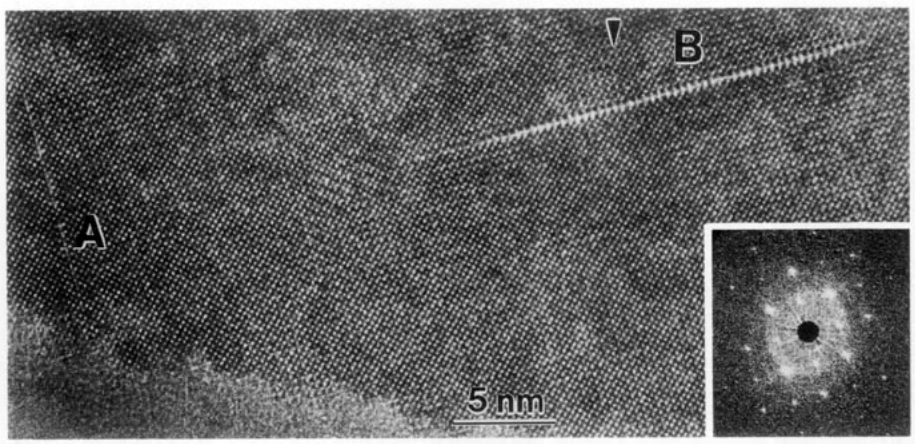

FIG. 6. ⟨100⟩ HREM image of the TEM specimen edge with two defects *A* and *B* on {100} planes. The defects exhibit a characteristic bright line which is one atomic layer thick. The inserted optical diffractogram was obtained from the amorphous specimen edge and indicates a defocus $\Delta f = -20 \pm 5$ nm.

One-third of the oxygen atoms are positioned in the La/Sr columns while the other oxygen atoms lie in two columns in-between the Mn columns. The projected crystal is shown in Fig. 8 together with simulated images for $-50 \leq \Delta f \leq -20$ nm and $1.1 \leq t \leq 7.6$ nm. For the calculated images a supercell (slice thickness 0.5459 nm, sampling 256 × 128) was chosen which contains a planar defect on a (100) plane. A complete atomic layer of La/Sr cations was removed (see double arrows in Fig. 8). The oxygen atoms remained in this specific layer. In the perfect crystal structure, only the positions of the La/Sr columns give rise to pronounced dark dots for $-45 \leq \Delta f \leq -35$ nm and $1.1 \leq t \leq 2.7$ nm. The plane containing the Mn and O columns appears as a uniform line with slightly brighter contrast than the dark dots. The tunnels between the La/Sr columns can be recognized by a characteristic bright dumbbell contrast at $-50 \leq \Delta f \leq -40$ nm and $1.1 \leq t \leq 2.7$ nm. With increasing thickness this dumbbell contrast changes into broad bright contrast bands and the dark dots of the La/Sr columns vanish, while the plane with Mn columns form dark contrast bands. In Fig. 8 it is interesting to note that the intensity only slightly increases at the positions of the La/Sr columns in the defective layer for $-50 \leq \Delta f \leq -40$ nm and $1.1 \leq t \leq 2.7$ nm. The major contrast contribution at the defect position is a strong increase of the dumbbell intensity. This is also true for $t = 4.9$ nm in the same defocus range. Images of a defect with a completely vacant Mn cation layer were calculated for the same defocus and thickness range and showed that the contrast is completely different (Fig. 10c). The contrast of the missing Mn layer reveals bright dots at the Mn columns and dark dots at the O columns ($-45 \leq \Delta f \leq -40$ nm, $1.1 \leq t \leq 2.7$ nm).

The experimental ⟨110⟩ HREM image of the defect is shown at low magnification in Fig. 9. The inserted optical

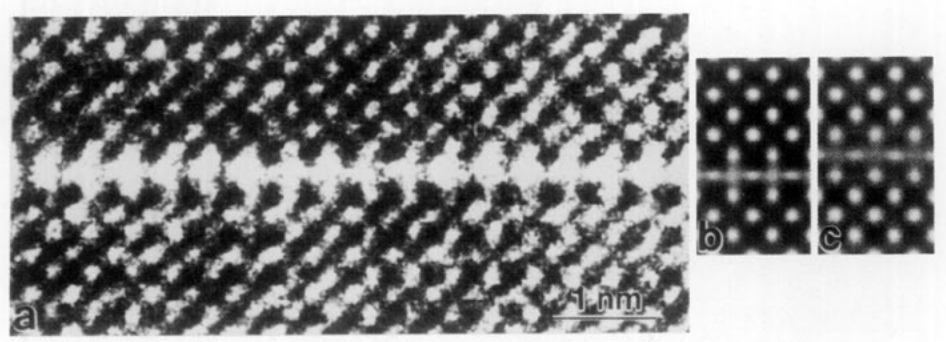

FIG. 7. (a) Higher magnification of defect *B* in Fig. 6. (b) Calculated image of a La/Sr vacancy defect with zero cation occupancy (best match $\Delta f = -20$ nm, $t = 3.5$ nm). (c) Calculated image of a Mn vacancy defect with zero cation occupancy (same imaging conditions as in (b)).

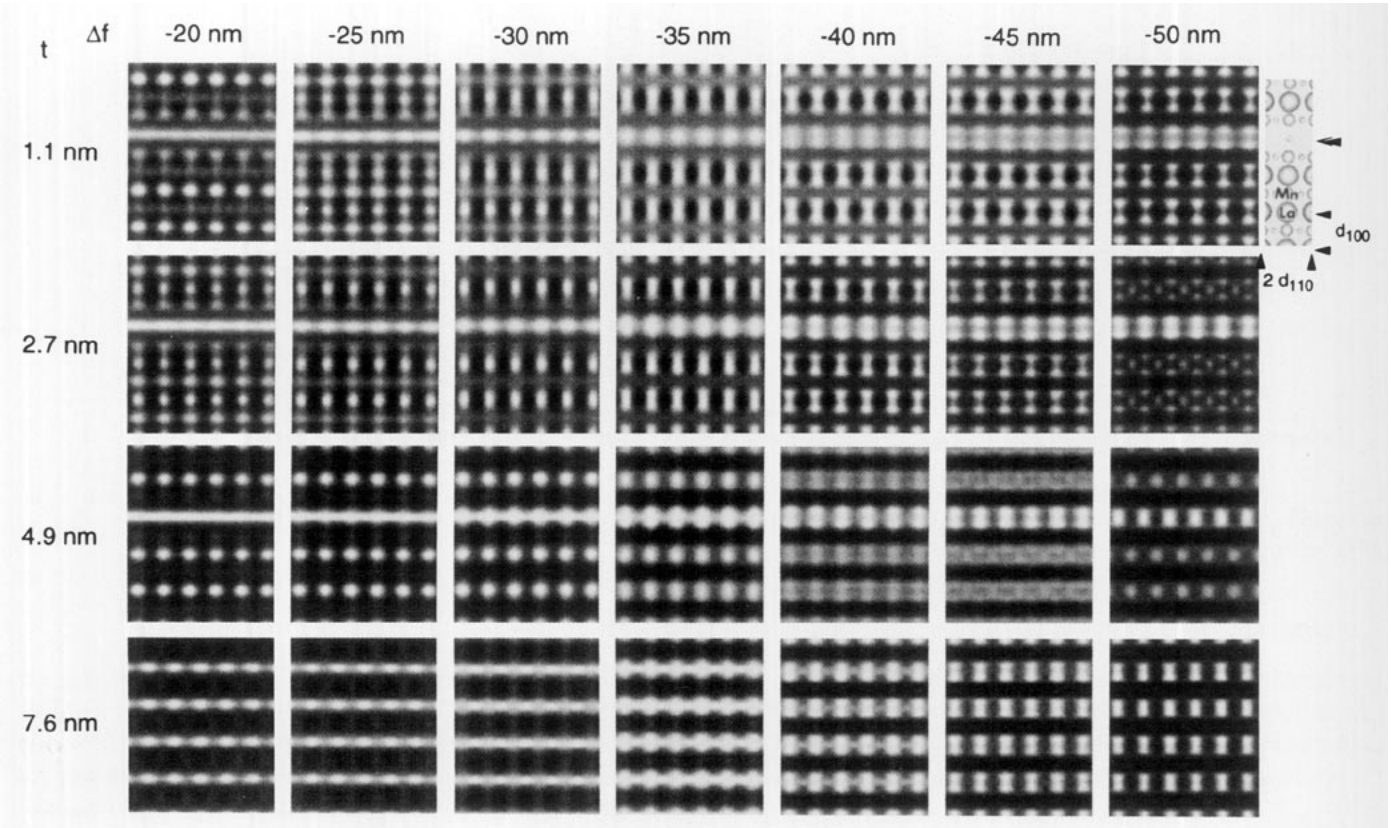

FIG. 8. Calculated ⟨110⟩ HREM images containing a La/Sr vacancy defect (zero occupancy) for various defoci and specimen thicknesses. The ⟨110⟩ projected crystal structure with the defect is shown to the right of the simulated images. Large atoms, La and Sr; medium atoms, Mn; and small atoms, O.

diffractogram obtained from the amorphous specimen edge indicates a defocus of $\Delta f = -40 \pm 5$ nm. In the higher magnified image (Fig. 10a) the rows with the bright dumbbells in the perfect crystal become clearly apparent. At the location of the defect their intensity increases enormously revealing the presence of a La/Sr vacancy defect. The best match ($\Delta f = -40$ nm, $t = 2.7$ nm) is shown in Fig. 10b. For comparison, the calculated image of a Mn vacancy defect is displayed in Fig. 10c. Compared to the ⟨100⟩ HREM images the defect shows a more pronounced

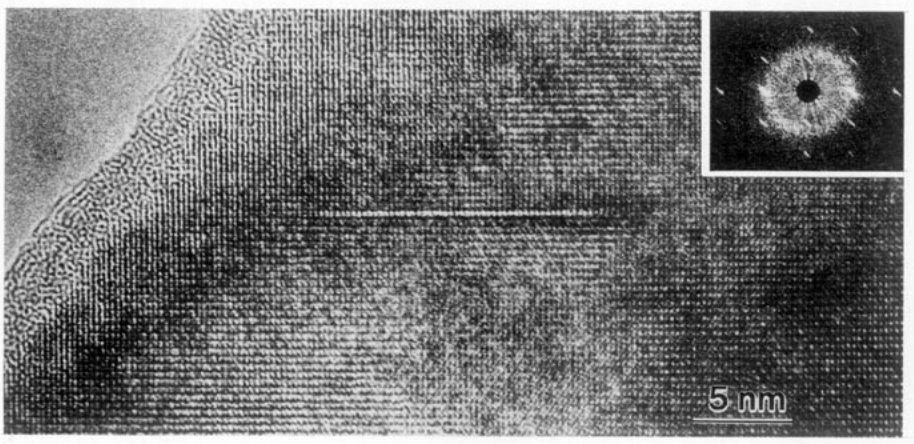

FIG. 9. ⟨110⟩ HREM image of the TEM specimen edge with one defect close to the edge. The defect exhibits characteristic bright dumbbells. The inserted optical diffractogram was obtained from the amorphous specimen edge and indicates a defocus $\Delta f = -40 \pm 5$ nm.

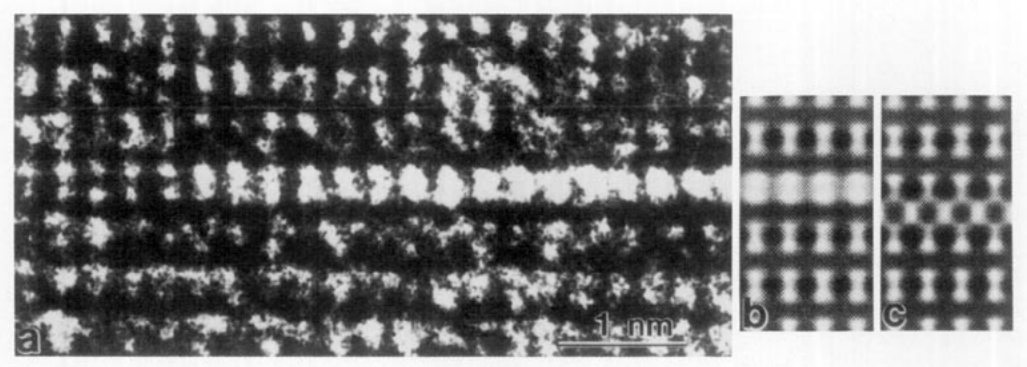

FIG. 10. (a) Higher magnification of the defect in Fig. 9. (b) Calculated image of a La/Sr vacancy defect with zero cation occupancy (best match $\Delta f = -40$ nm, $t = 2.7$ nm). (c) Calculated image of a Mn vacancy defect with zero cation occupancy (same imaging conditions as in (b)).

contrast and therefore is more easily identified in ⟨110⟩ projection.

3.4. Sensitivity of the HREM Contrast to the La/Sr Occupancy

The simulated images of the vacancy defect in Figs. 7b, 7c, 8, 10b, and 10c were carried out for zero cation occupancy. To test the sensitivity of the image contrast on the concentration of La/Sr atoms in the cation columns of the defect, images were calculated for 75, 50, and 25% La/Sr occupancy. Such a series of ⟨100⟩ images is shown in Fig. 11 for the imaging conditions $\Delta f = -20$ nm and $t = 2.3$ nm. The La/Sr vacancies become visible for a 50% occupancy. At a thickness of $t = 2.3$ nm this corresponds to three La/Sr vacancies. Comparing the intensity of the bright lines formed at the position of the defective atomic layer with the experimental image in Fig. 7a, it is concluded that a complete La/Sr layer is missing.

Figures 12a–12d show that the ⟨110⟩ images ($\Delta f = -40$ nm, $t = 2.7$ nm) are more sensitive since the intensity of the bright dumbbells increases already for a 75% La/Sr occupancy. This means that one or two vacancies may be detected in a La/Sr column, containing seven cations positions at $t = 2.7$ nm in ⟨110⟩ projection. Also in this case a comparison with the experimental image in Fig. 10a suggests that the defect corresponds to zero La/Sr occupancy.

4. DISCUSSION

From the excellent match of a simulated ⟨110⟩ image of a pure La/Sr defect (Fig. 10b) with the experimental ⟨110⟩ image (Fig. 10a), the planar defects were identified as La/Sr vacancy defects. It has been shown that ⟨110⟩ HREM images under specific imaging conditions are better suited than ⟨100⟩ images to distinguish La/Sr from Mn vacancy defects in LSM. Further image simulations of the ⟨110⟩ projection under these specific imaging conditions showed that a pure O vacancy defect would not produce the same image contrast. Certainly the charge of the missing La/Sr cations will have to be compensated. This occurs probably via the anion lattice by the generation of O vacancies and by the oxidation of Mn^{3+} cations in the layers next to the defect. The defects in the bright-field image of Fig. 1 display also a strain field contrast which indicates that the missing La/Sr columns cause a local relaxation of the lattice.

The defects have a mean diameter of about 25 nm and their density was determined to be 5×10^{16} cm^{-3} (Fig. 1). One atomic (100) monolayer of *A* or *B* cations contains 6.7×10^{14} atoms/cm^2, while 1.75×10^{22} atoms/cm^3 make up stoichiometric $La_{0.8}Sr_{0.2}MnO_3$. For zero La/Sr occupancy the number of La/Sr vacancies accommodated in the defects corresponds to approximately 1% of the La/Sr atoms in stoichiometric LSM. Other La/Sr vacancies

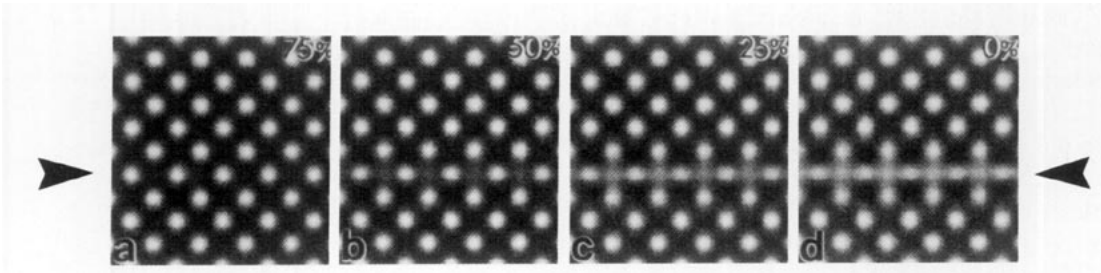

FIG. 11. Sensitivity of ⟨100⟩ HREM images ($\Delta f = -20$ nm, $t = 2.3$ nm) to the La/Sr occupancy: (a) 75, (b) 50, (c) 25, and (d) 0% occupancy. The arrow indicates the position of the defective La/Sr plane.

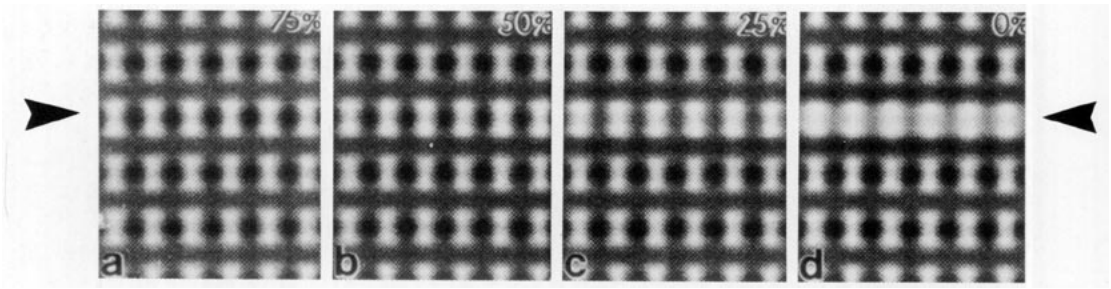

FIG. 12. Sensitivity of ⟨110⟩ HREM images ($\Delta f = -40$ nm, $t = 2.7$ nm) to the La/Sr occupancy: (a) 75, (b) 50, (c) 25, and (d) 0% occupancy. The arrow indicates the position of the defective La/Sr plane.

could be present in the form of point defects which are not visible in TEM images. At this point it is noted that all diffraction patterns of the ⟨110⟩ and ⟨112⟩ zone axes revealed additional 1/2{111} spots which are not an intrinsic feature of the cubic perovskite or trigonal (R-3c) structure and are not revealed in X ray diffraction patterns. Currently it is under investigation whether in LSM these spots could be associated with vacancy ordering in either the cation or anion sublattice.

An absolute quantitative measurement of the fraction of vacancies in individual La/Sr columns would require a thorough study of the linear and nonlinear interactions of transmitted and diffracted beams and their contributions to the image contrast. A quantitative measurement of Al atoms or vacancies in mixed Ga/Al columns at Al(Ga)As/GaAs heterostructure interfaces was described in this way [12–14]. When studying quantitatively atom concentrations at an interface, the image contrast of the adjacent layers may be used as references. This is, however, not possible in the present case. For an unknown, one-atomic-layer-thick vacancy-type defect in a well-known matrix, it is necessary to compare intensities of calculated images quantitatively with those of experimental images. This will become possible when inelastically scattered electrons are filtered and charged coupled device (CCD) detectors which have a highly linear response to electron intensities are used to record digitized images [15].

5. CONCLUSION

The HREM contrast in ⟨100⟩ and ⟨110⟩ projections of planar La/Sr vacancy defects, one atomic layer in thickness, was studied experimentally in a 400 kV TEM and by image simulations. In both imaging directions imaging conditions (Δf, t) could be found which make it possible to distinguish a La/Sr from a Mn vacancy defect. The difference in the contrast is more evident from the image features occuring in the ⟨110⟩ than in the ⟨100⟩ projection. Also the sensitivity of the contrast to the La/Sr occupancy is higher in ⟨110⟩ images. A La/Sr occupancy of only 75% already gives rise to a pronounced contrast. A qualitative comparison of experimental and calculated ⟨110⟩ images suggests that the defects are pure La/Sr vacancy defects with probably almost zero cation occupancy. The material under investigation contains a high density of planar defects which accomodate approximately 1% La/Sr vacancies. The ⟨110⟩ projection and the imaging conditions $\Delta f = -40$ nm, $t = 2.7$ nm should be used in the future to identify vacancy defects in $La_{0.8}Sr_{0.2}MnO_3$. It is of importance to study defect-structure/composition relations by HREM since the physical properties and the chemical reactivity of $La_{0.8}Sr_{0.2}MnO_3$ will change with deviations from the cation or anion stoichiometry as it is typical for metal oxides adopting the perovskite or perovskite-related structures.

ACKNOWLEDGMENTS

The author thanks R. Männer for providing the sample, O. Eibl for valuable discussions, M. Schiele for TEM specimen preparation, T. Fuska for photographic work, and H. Oppolzer for critical reading of the manuscript.

REFERENCES

1. F. S. Galasso, "Perovskites and High-T_C Superconductors." Gordon and Breach, New York, 1990.
2. B. C. H. Steele, *Bull. Mater. Res. Soc.* 19 (June 1989).
3. E. Ivers-Tiffeé, W. Wersing, M. Schießl, and H. Greiner, *Ber. BunsenGes. Phys. Chem.* **94,** 978 (1990).
4. A. Hammouche, E. J. L. Schouler, and M. Henault, *Solid State Ionics* **28–30,** 1205 (1988).
5. B. C. Tofield and W. R. Scott, *J. Solid State Chem.* **10,** 183 (1974).
6. A. Reller, *Phil. Mag. A* **68,** 641 (1993).
7. M. Schießl, E. Ivers-Tiffeé, and W. Wersing, *in* "Ceramics Today–Tomorrow's Ceramics" (Vincenzini, Ed.). pp. 2607–2614. Elsevier, Holland, 1990.
8. A. Iberl, Thesis, Universität Regensburg, Germany, 1991.
9. A. Hammouche, E. Siebert, and A. Hammou, *Mater. Res. Bull.* **24,** 367 (1989).
10. P. A. Stadelmann, *Ultramicroscopy* **21,** 131 (1987).
11. F. Thon, *Z. Naturforsch.* **21a,** 476 (1966).
12. A. Ourmazd, F. H. Baumann, M. Bode, and Y. Kim, *Ultramicroscopy* **34,** 237 (1990).
13. S. Thoma and H. Cerva, *Ultramicroscopy* **35,** 77 (1991).
14. S. Thoma and H. Cerva, *Ultramicroscopy* **38,** 265 (1991).
15. S. Kujawa and D. Krahl, *Ultramicroscopy* **46,** 395 (1992).